

**Fig. 1** (a) Chemical structure of the conjugated polymer P3HT and the solid state ionic liquid [C<sub>1</sub>C<sub>12</sub>IM<sup>+</sup>][PF<sub>6</sub><sup>-</sup>] (SSIL). Normalised absorbance spectra of P3HT neat, 1:1 and 1:5 for (b) low  $M_w$  and high RR, (c) high  $M_w$  and low RR and (d) high  $M_w$  and RR P3HT blends.

cause difficulties in realising efficient devices; instead, they often have slow turn-on and require prebiasing.<sup>14</sup> Recently, the development of a solid-state ionic liquid (SSIL) with matching surface energy and stable ion diffusion has been shown to significantly improve device performance.<sup>9</sup>

In this respect, herein, we examine a novel  $\pi$ -conjugated polymer/solid-state ionic liquid complex, to realize a simple solid-state device for potential gas sensing applications. This study aims to investigate the properties of the ionic liquid blend using the different chemical and physical properties of a model organic polymer, P3HT (Fig. 1a), which is a widely used semiconductor polymer. Owing to its commercial availability, it is the ideal polymer to use in novel devices. There is already a wealth of knowledge of the characteristics and fabrication processes of P3HT, allowing it to be easily scaled up in new technologies.<sup>15</sup> Controls over the polymer chain length and side chain positioning allow the study of the effects of the molecular order and crystallinity. With a greater understanding of how the blend mechanism works, there is a greater potential for fine-tuning the performance and opening up a variety of different applications. Furthermore, we identify the electric-field driven chemical interactions between P3HT and the SSIL at a molecular level and their electrostatic interactions with the exposed VOC using an assay of advanced structural and optical spectroscopic techniques such as *in situ* resonant Raman spectroscopy and high-angle annular dark-field scanning transmission electron microscopy.

## Results and discussion

The molecular weight ( $M_w$ ) dependence of the P3HT:SSIL blend was tested within the range of 10–160 kg mol<sup>-1</sup>, with a regio-regularity (RR) of around 95%. The normalised absorbance

values of the neat and blended films of 10 kg mol<sup>-1</sup> 95% regio-regular P3HT (RR-P3HT) (low  $M_w$ , high RR) and 58 kg mol<sup>-1</sup> 96% RR-P3HT (high  $M_w$ , high RR) are shown in Fig. 1b and d, respectively. RR-P3HT shows a broad absorbance with a peak at 504 nm. When the molecular weight is increased, the absorption shows a redshift to 549 nm and an increase in the relative intensity of the 600 nm shoulder. This is an indication of an increased conjugation length and a higher molecular order.<sup>16</sup> The effect of regio-regularity was examined using P3HT samples of fixed  $M_w \approx 60$  kg mol<sup>-1</sup> and regio-regularities of 50–99%. Fig. 1c shows the absorbance of 57 kg mol<sup>-1</sup> 65% regio-random P3HT (RRa-P3HT) (high  $M_w$ , low RR). At a low regio-regularity, the P3HT absorption shows a broad featureless absorption at a lower wavelength of 454 nm. In RRa-P3HT films, the randomly oriented side chains prevent stacking and reduce interchain interactions.<sup>17</sup> The molecular weight and crystallinity dependence of P3HT absorbance has been well reported in the literature.<sup>16–19</sup> The main features in the absorbance are observed between 500 and 600 nm and are attributed to both intra- and interchain interactions.<sup>20,21</sup> Herein, our study connects such molecular weight and regio-regularity dependence of P3HT with their electrical properties in a simple 2-terminal diode architecture and the efficiency of intermolecular interactions (particularly, doping) with the SSIL for chemical gas sensing applications.

Optical absorption transition bands are dependent on the doping level of polymers.<sup>22</sup> Under doped conditions, ground-state absorption peaks show significant bleaching as the proportion of the neutral polymer decreases with the concomitant appearance of a broad sub-bandgap absorption known as the polaronic band.<sup>23</sup> The normalised absorbance (see Fig. 1b–d) of the P3HT:SSIL blend was used to examine the chemical doping and the influence of the SSIL on the P3HT electronic and morphological conditions. Since the SSIL has no absorption peaks in the visible range (Fig. S1 in the ESI<sup>†</sup>), any changes in the absorbance can be attributed to the electrostatic interactions and/or changes in the morphology of P3HT by the SSIL, however, not of the SSIL itself. The absorbance of the neat P3HT film compared to the 1:1 and 1:5 (P3HT:SSIL) blends is shown in Fig. 1b–d. There is no presence of any measurable sub-bandgap absorption, showing that the SSIL does not chemically dope P3HT in the ground state.<sup>24</sup> Fig. 1b and c show that, at low  $M_w$  and RR, blending with the SSIL shows minor changes to the overall absorbance with some broadening of the main peak at low wavelengths. This implies that the SSIL has only minor effects on the packing of the P3HT chains. Fig. 1d shows that P3HT with high  $M_w$  and RR shows an increase in the 600 nm shoulder as the blending ratio increases. This greater impact on the absorption characteristics suggests that it has a greater effect on the polymer interchain packing in comparison to lower  $M_w$ . The stronger vibronic shoulder at 600 nm is an indication of a higher molecular order.<sup>25,26</sup> Such increases in relative absorbance suggest that blending with the SSIL increases the P3HT molecular order in the film, which is expected to have major impacts on the efficiency of intermolecular interactions between the SSIL and P3HT, resulting in different charge transport properties, as discussed below.



## Electrical properties of P3HT:SSIL blends

The electrical performance of the P3HT and blends was compared *via* source–drain current measurements in a two-terminal diode architecture, chemiresistor (see Fig. 2a). Any changes in the electrical currents upon exposure to a given chemical gas are an indication of the presence of the analyte, *i.e.*, a sensing response is measured by fluctuations in the resistance upon the interaction of the film with the given analyte.<sup>27,28</sup> This architecture is particularly useful for studying the charge conduction of a semiconductor and the specific sensing mechanism of each system.<sup>29,30</sup> Fig. 2b shows the driven voltage-dependent currents across the neat and blended devices (with focus on the low-voltage regime, useful for low power devices). P3HT with both low  $M_w$  and RR shows no dependence on the applied voltage and measure a current of  $10^{-10}$  A even under significant applied voltages of up to  $-60$  V. When blended with the SSIL, the current is not enhanced showing that the ionic liquid blend has no positive effect on the conductivity of P3HT with low  $M_w$  or RR. At high  $M_w$  and RR, the neat P3HT film measures a current of  $10^{-8}$  A at  $-0.1$  V, which increases linearly with applied voltages following Ohm's law. When blended with the SSIL at a ratio of 1 : 1, there is an enhancement of the current level across all applied voltages, showing increased conductivity in the blended film. Blending with the SSIL also reduced the contact resistance and channel resistance by orders of magnitude from  $M\Omega$  to  $k\Omega$  ensuring more efficient charge injection and charge transport (Fig. S2 in the ESI†).

Fig. 2c summarises the electrical properties of P3HT dependent on its molecular weight (with the regioregularity shown in Fig. S3 in the ESI†). Here, mean currents are extracted from the driven voltage-dependent measurement at  $-2$  V to compare across molecular weight, regioregularity, and the blending ratio. For the neat P3HT film, the current level increases from low  $M_w$ , saturating at around  $40 \text{ kg mol}^{-1}$ , after which the extracted current level remains constant at  $10^8$  A. This correlates well with the previously reported critical molecular weight ( $M_c$ ) of  $34 \text{ kg mol}^{-1}$  for P3HT, where the molecular packing changes from chain extended crystals to interlinked regions of crystalline lamellae.<sup>31</sup> At low  $M_w$ , the SSIL blend shows a decrease in the current level for a high blending ratio and no enhancement when blended 1 : 1. When  $M_w$  is increased to  $40 \text{ kg mol}^{-1}$  both the 1 : 1 and 1 : 5 blends show increases in current levels under applied voltages. The P3HT : SSIL (1 : 1) blend with  $M_w = 58\text{k}$  and RR = 96% shows

the best performance in the driven voltage dependence test, measuring a mean current of  $7 \times 10^{-5}$  A, which is three orders of magnitude greater than that of the corresponding neat film. The driven voltage dependence shows a clear increase in electrical performance when blended with the SSIL at high  $M_w$  and RR, showing a beneficial interaction with the SSIL. As previously discussed (*via* absorbance in Fig. 1b–d), such electrical current increases are not linked with ground-state chemical doping, suggesting a plausible link with electric field induced doping instead, which will be discussed in detail later (Fig. 5).

## Thin film morphological characteristics

High angle annular dark-field scanning transmission electron microscopy (HAADF-STEM) was used to analyse and compare the morphology of the lowest  $M_w$  and the optimal electrical performance,  $58 \text{ kg mol}^{-1}$  (see Fig. 3). The neat films, shown in Fig. 3a and d for low  $M_w$  ( $10 \text{ kg mol}^{-1}$ ) and high  $M_w$  ( $58 \text{ kg mol}^{-1}$ ), show no features with little distinctive difference in morphology. However, the morphology of the low  $M_w$  1 : 1 blended film (Fig. 3b) shows isolated large white regions on a darker background. Elemental profile scanning along the line indicated in Fig. 3c and shown in Fig. 3g can be used to examine the distribution of the two moieties in the blended film. The profile measures the proportion of P3HT by the sulphur atoms (from the thiophene ring) and the phosphorus and fluorine atoms (from the  $\text{PF}_6^-$  anion of the SSIL). This shows that the white isolated regions of the HAADF-STEM image in Fig. 3b essentially contain only P3HT with roughly 70 counts for sulphur compared to a count below 10 for both phosphorus and fluorine, while the surrounding dark regions measure 40 counts of both phosphorus and fluorine with no sulphur. This suggests that the low molecular weight P3HT forms localised aggregates and exhibits little intermixing with the SSIL. This correlates with the very minor changes in absorbance (discussed previously in Fig. 1) observed at low  $M_w$ ; due to the segregation of the polymer and SSIL, there are minor changes to the environment for the majority of P3HT inside the aggregates and therefore no significant change in the absorbance. The morphology is confirmed on a more macroscopic scale by observing the film topography under a microscope and an atomic force microscope (Fig. S4 and S5 in the ESI†). Such fragmented nature of the semiconductor explains why the conductivity of the film is

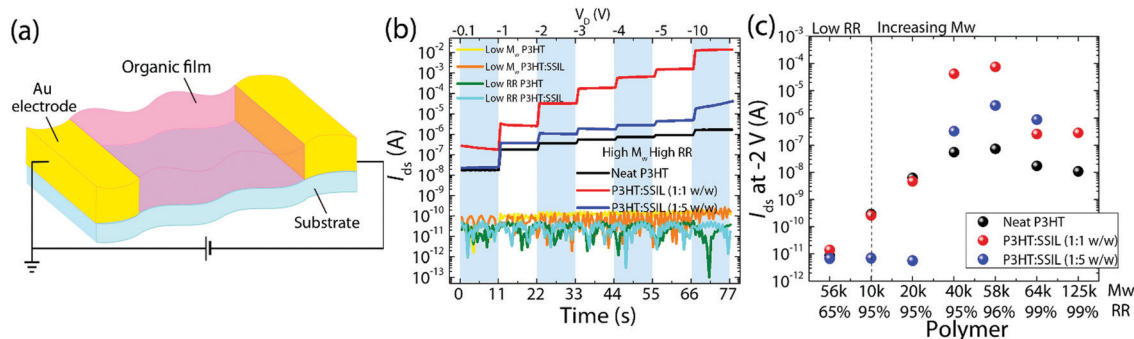


Fig. 2 (a) Diagram of the chemiresistor device structure; (b) driven voltage dependence across the  $L = 5 \mu\text{m}$  and  $W = 2 \text{ mm}$  chemiresistor channel and (c) mean drain current measured for each polymer under an applied bias of  $V_D = -2$  V.







The fine discriminatory abilities of the P3HT:SSIL blend are highly comparable and even superior to those of previously reported organic chemiresistors (Tables S1 and S2 in the ESI†).

Blending P3HT with the SSIL is shown to enhance the electrical properties of the chemiresistor (discussed previously in Fig. 2) which in turn increases the gas sensing response and introduces sensitivity between gas analytes. The effectiveness of the blend is determined by the molecular weight and regio-regularity of the polymer. The molecular weight must exceed a critical value before the electrochemical doping properties of the SSIL are activated. A high regioregularity is required, suggesting that a higher degree of crystallinity is necessary to undergo the interaction with the SSIL. Both  $M_w$  and RR have a strong influence on the packing and morphology of the polymer chains, which in turn influences how the SSIL intermixes with P3HT and how the resulting thin film depends on the aggregation and packing of P3HT. This shows that the optimum P3HT:SSIL morphology is an interconnected P3HT pathway with a higher surface area and high conductivity. However, these methods are not able to give the full picture of what is happening at the molecular level and how the ions interact with the polymer chain.

### Correlating device currents with electric field-dependent doping of the polymer by the SSIL

The specifics of device current measurements of the neat P3HT and P3HT:SSIL (1:1) blend chemiresistors are shown in Fig. 5a, while the concomitant *in situ* molecular probing *via* resonant Raman spectroscopy is shown in Fig. 5b and e for neat and blended films, respectively.<sup>9,22,23,36–38</sup> For the neat device, the current increases linearly with the applied field with respect

to Ohm's laws. For the blend, however, the current initially increases with respect to the same principle, followed by strong injection current turn-on at  $-1.3$  V resulting in an order of magnitude higher currents compared to the neat P3HT film. Such field-dependent conductivity tuning is expected to originate from intermolecular interactions between P3HT and the SSIL, and thus Raman spectroscopy was conducted to gain insights into the chemical structure, molecular conformation, and  $\pi$ -electron density distribution in P3HT.<sup>39</sup> The normalised Raman spectroscopy (Fig. S8 in the ESI†) shows that blending with the SSIL does not affect peak positions or relative intensities compared to the neat P3HT film. This confirms the absence of ground state doping (also shown by the absorbance spectra in Fig. 1) and additionally indicates that blending with the SSIL does not affect the molecular conformation of the  $\pi$ -conjugated backbone of P3HT.

As the P3HT:SSIL blends show stark enhancements of the electrical currents under applied voltages, *in situ* field-dependent resonant Raman spectroscopy (FDRS) was performed under device operating conditions. The FDRS of chemiresistors was conducted under 785 nm excitation, which is non-resonant with the ground-state absorption and resonant with the polaronic absorption of P3HT.<sup>23</sup> The main features of the P3HT Raman signal are the C=C symmetric stretching mode ( $1450\text{ cm}^{-1}$ ) and the C-C intraring mode ( $1378\text{ cm}^{-1}$ ).<sup>40</sup> For the neat P3HT film (58k 96% RR) (Fig. 5b), the Raman signal at 0 V resembles the open-circuit steady-state Raman one, and, with increasing drain voltages, there are no differences in the peak positions or relative intensities, clarified by the 2D Raman plots of absolute Raman intensity with Raman shift (abscissa) and applied voltage (ordinate) (Fig. 5c). Interestingly, Fig. 5e shows that the blend demonstrates drastically different behaviour, with a significant

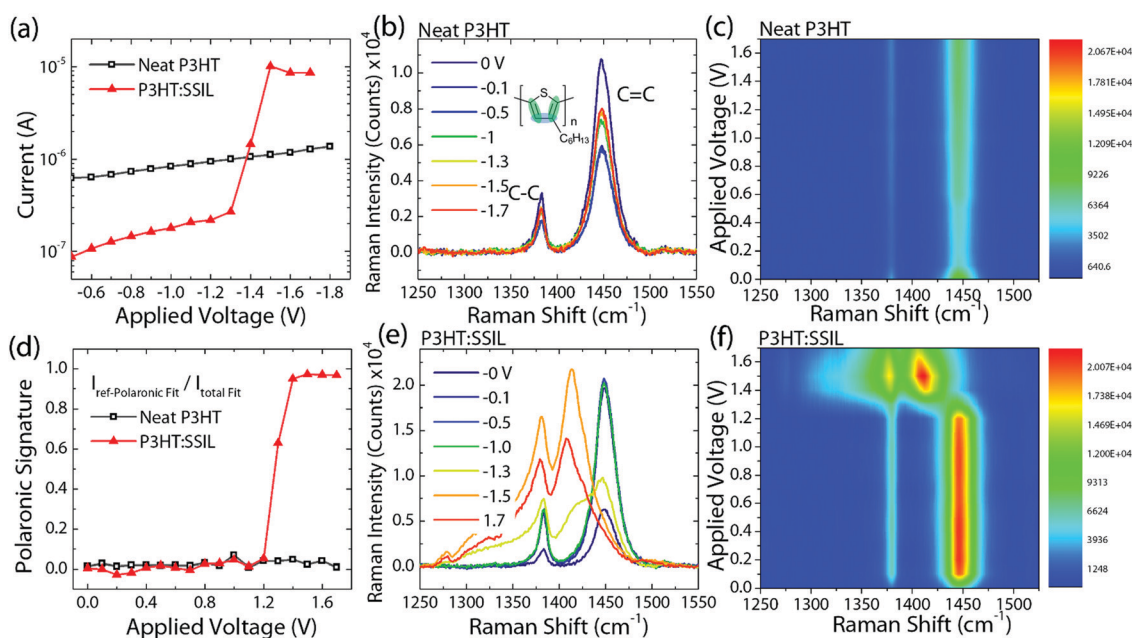


Fig. 5 *In situ* field-dependent Raman spectroscopy (FDRS) of neat P3HT and the P3HT:SSIL 1:1 blend. (a) current measured during FDRS. FDRS for (b) neat P3HT and (e) the P3HT:SSIL blend. 2D Raman intensity plot at different applied voltages for (c) neat P3HT and (f) the P3HT:SSIL blend. (d) Polaronic signature fitted by a linear combination of the reference neutral and polaronic P3HT Raman peaks.



spectral transition at  $-1.3$  V (the same voltage for current injection turn-on, discussed previously in Fig. 5a). Such a spectral transition is seen more clearly in the corresponding 2D Raman plots of the blend (see Fig. 5f). These dramatic changes in the Raman signal were also shown to be reversible upon the removal of the applied voltage (Fig. S9 in the ESI†) and highly reproducible (Fig. S10 in the ESI†).

The mechanics of the Raman spectral changes for neat and blend devices is shown by the evolution of the peak positions and intensities under applied voltages (Fig. 5b and e; see Fig. S11 in the ESI† for more details). For the neat P3HT film, the initial absolute Raman peak intensity decreases (uniform for both C–C and C=C peaks), followed by steady increases with applied voltages (note however that the changes are minimal and within 50% of the initial value at 0 V). This is completely different for the blends, where a significant increase, particularly for the C–C peak, is observed beyond  $-1.2$  V (a clear indication of field-induced interactions originating from the presence of the surrounding SSIL). Likewise, a frequency downshift by  $\approx 40$   $\text{cm}^{-1}$  (from 1450 to 1410  $\text{cm}^{-1}$ ) for the C=C peak is observed only in the blends beyond  $-1.2$  V, indicating molecular lattice reorganisation (here, corresponding to an enthalpic loss of  $\approx 5.1$  meV). We notice that the Raman spectral signature beyond  $-1.2$  V closely resembles hole-polaronic Raman spectra (*i.e.* the P3HT polymer with sufficient hole-polarons  $> 10^{20}$   $\text{cm}^{-3}$ ), also reported previously by Nightingale *et al.*<sup>23</sup> in an electrochemical cell. Refer to Fig. S12 in the ESI† for the reference neutral and hole-polaronic Raman spectra acquired *in situ* for an electrochemical cell. Thus, the Raman spectrum transitions from a neutral P3HT signature (*e.g.* at 0 V) to a hole-polaronic P3HT signature (*e.g.* at  $-1.7$  V), where the transition turn-on occurs at  $-1.3$  V, originate from the intermolecular electric field-induced doping of P3HT by the SSIL (termed as electrochemical doping). Understandably, the molecular lattice relaxation occurs due to an increase in hole polarons in the polymer leading to frequency downshift particularly of C=C, *i.e.*, an increase in the bond length and acquiring a more C–C like character (the lowering of the  $\pi$  electron density and force constant as the C=C bond changes to be more single bond-like).<sup>41</sup> Likewise, the peak intensity of the intraring C–C bond (1378  $\text{cm}^{-1}$ ) increases as the  $\pi$  electron density increases.<sup>41</sup> It has been suggested that there is a decrease in the Raman signal after the peak polaronic performance (at  $-1.5$  V, see Fig. 5e) associated with the formation of doubly charged states, known as bipolarons, which are not resonant at 785 nm.<sup>42</sup>

The experimentally obtained field-dependent Raman spectra in Fig. 5b and e can be fitted by a linear combination of the reference neutral and polaronic P3HT Raman peaks (see Fig. S13 in the ESI†) to obtain the polaronic signature fraction given by  $I_p/(I_p + I_n)$ , where  $I_p$  and  $I_n$  are the integrated intensity of the polaronic spectral fit and neutral spectral fit, respectively. The resulting polaronic signature fraction represents the closeness of the polaronic or neutral spectral shape, where 1 corresponds to a 100% polaron P3HT shape while 0 corresponds to a 100% neutral P3HT shape. The polaronic signature fraction against applied voltages for neat and blended films shown in Fig. 5d clearly

shows the formation of hole polarons in the polymer for blends. The trend closely correlates with the device currents (previously discussed in Fig. 5a). As the current density  $J = ne\mu E$ , where elementary charge ( $e$ ) and electric field ( $E$ ) remain constant, it can be inferred that the transition point at  $-1.3$  V is influenced by either the charge carrier density ( $n$ ) or the charge mobility ( $\mu$ ). As an increase in the Raman intensity of the polaronic peaks is linked with an increase in the number of charges present,<sup>23</sup> it can be concluded that the current injection turn-on is more likely to be contributed by an increased number density of holes travelling through the film. The blend shows two regimes in the charge transport characteristics. As a low voltage is applied, the current flows through the film, which is in line with the increase in the electric field. There is a steady increase in the current measured and an increase in the polaron resonant intensity but no structural change. In the second phase, once the number of charge carriers in the film has increased beyond the threshold charge density, the polymer starts to undergo structural changes, indicative of a high polaron density.

### VOC induced molecular interactions

We now investigate the VOC induced effect on the molecular properties of the P3HT:SSIL blend devices, focussing on the exposure to acetone and toluene (see Fig. 6). The blend device's VOC selectivity towards the discrimination of acetone and toluene in *in situ* Raman measurement was same as that observed at lower VOC concentration (discussed previously in Fig. 4). The P3HT:SSIL blend shows a strong positive change in resistance under acetone exposure and a negative change under toluene exposure. The relative response time of acetone and toluene is more prominent than that at a lower concentration, where much faster negative response and recovery are seen when toluene is introduced into the sample chamber.

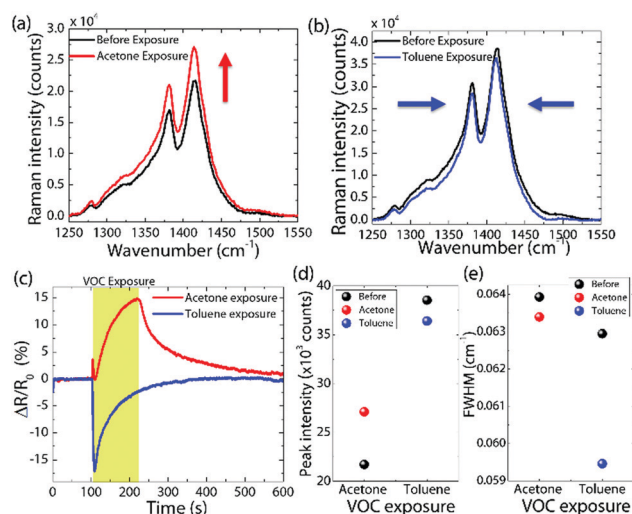


Fig. 6 *In situ* Raman spectroscopy under VOC gas exposure for the 1:1 P3HT:SSIL blend in the presence of (a) acetone and (b) toluene. (c) Percentage change in electronic resistance under acetone and toluene exposure upon the injection of a high concentration of the VOC under an applied voltage of 4 V. (d) Peak intensity (the C=C mode) and (e) FWHM of P3HT:SSIL before and after VOC exposure.





The blend device shows the P3HT polaronic features under bias (4 V) before VOC exposure due to the interaction between the polymer and ionic liquid (discussed above). When the film is exposed to acetone, there is an increase in the overall intensity of Raman peaks (Fig. 6a) with no change in the peak position or relative intensity. In contrast, when exposed to toluene, the Raman signal shows a decrease in intensity and a narrowing of the FWHM (Fig. 6b). The narrowing of the peak suggests an increase in the P3HT molecular order<sup>25</sup> which in turn results in a closer packing and faster charge transfer in the device.<sup>43</sup> On the other hand, the Raman signal increase is associated with an increase in the polaron density present in P3HT. However, this increase does not improve the measured conductivity of the device upon exposure to acetone, suggesting potential trapping of polarons in P3HT by acetone.<sup>44</sup>

Based on the optical, morphological and electrical results obtained for the P3HT:SSIL blend, we hypothesise the transduction sensing mechanisms under different VOCs (Fig. 7). In the case of a high molecular weight neat P3HT film, the polymer chains are highly ordered in an interlinked lamellar packing. The conduction of charges through the film occurs by a mixture of intrachain along polymer chains including along the molecules between different lamella and by interchain hopping mechanisms.

When P3HT is blended with the SSIL the morphology changes to create an interpenetrating network of P3HT pathways through the film. The electrochemical interaction of P3HT with the SSIL forms long-lived polaronic P3HT states under applied voltages. When the device is exposed to the gas analyte, VOCs can be adsorbed into the film physically or chemically. Upon exposure to toluene, P3HT shows an enhanced molecular order and reduced device resistance, suggesting a strengthening of the interaction between P3HT and the SSIL. As toluene is a large non-polar gas

molecule with an aromatic ring, it is likely that it is adsorbed onto the porous film (*i.e.* physical adsorption), enabling proximity between polymer chains and the solid-state ionic liquids, increasing the P3HT molecular order and strengthening the electrochemical interactions between them.

In contrast, acetone is a smaller but highly polar gas molecule. When the blend is exposed to acetone there is an increase in device resistance and the response time is significantly slower. In this case, the negatively charged oxygen of the polar molecule can interact with the positively charged hole polarons in P3HT (*i.e.* chemical adsorption). Such an interaction can lead to the hole polaron in P3HT to be less mobile (*e.g.* trapped by the gas molecule), preventing effective transport to the electrode.<sup>45</sup> This mechanism accounts for the increase in polaron density probed by Raman but the lower conductivity measured in the device upon acetone exposure.

## Conclusions

In conclusion, we have demonstrated a highly sensitive and selective VOC gas sensor using  $\pi$ -conjugated polymer (P3HT)/SSIL blends. The polymer chain packing and resulting morphology in the blends are shown to be important to determine the degree of electrochemical interactions between P3HT and the SSIL. P3HT with high molecular weight and regioregularity forms an extremely well-interconnected network in blends desirable for efficient charge transport. In P3HT/SSIL blends, we have identified the electric-field driven strong chemical interactions between P3HT and the SSIL to tune the electrical conductivity of P3HT. The enlarged interfacial areas in blends and the solid-state nature of the SSIL ensure highly tuneable electrochemical interactions between them, efficiently modulating the electrical conductivity of P3HT further upon exposure to different polar and non-polar VOCs. Our results demonstrate the  $\pi$ -conjugated polymer/SSIL complex as a new highly sensitive and selective gas sensor platform and provide a key scientific understanding of its operational mechanisms at the molecular level, critical for developing molecular sensors towards next-generation non-invasive diagnostics.

## Experimental

### Materials

P3HT was purchased from 1 M having a range of molecular weights and regioregularities. To study the  $M_w$  dependence, a range of 10–160 kg mol<sup>-1</sup> was used with a regioregularity of around 95% and, to study the regioregularity dependence, the  $M_w$  was fixed at around 60 kg mol<sup>-1</sup> and regularities between 50 and 99% were used. Solid state ionic liquid 1-dodecane-3-methylimidazolium hexafluorophosphate ( $[\text{C}_{12}\text{IM}^+][\text{PF}_6^-]$ ) was synthesised through a conventional method described elsewhere.

### Film preparation

P3HT and SSIL blends were dissolved in chloroform at 5 mg ml<sup>-1</sup> and stirred at 40 °C. The solutions were filtered through a 0.45  $\mu\text{m}$  filter and left for 48 hours before being spin-coated

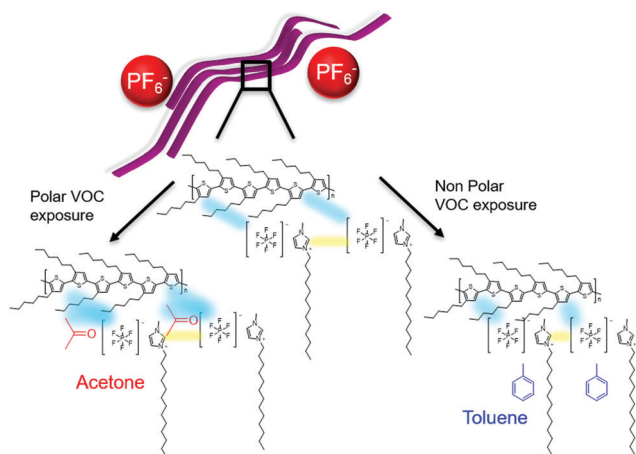


Fig. 7 Schematic diagram showing the hypothesised sensing mechanism of P3HT:SSIL under exposure to polar and nonpolar solvents. An electrochemical interaction (blue) occurs between the SSIL and the P3HT backbone as long-lived polaronic states. The strength of this interaction is modulated by the presence of the VOC. Acetone chemically adsorbs onto the film, trapping the polaronic states and preventing effective transport to the electrodes, while the physical adsorption of toluene shortens the distance between P3HT and SSIL, strengthening the interaction.







- 8 W. Hu, L. Wan, Y. Jian, C. Ren, K. Jin, X. Su, X. Bai, H. Haick, M. Yao and W. Wu, *Adv. Mater. Technol.*, 2019, **4**, 1–38.
- 9 H. Yan, S. Limbu, X. Wang, J. Nightingale, I. Hamilton, J. Wade, S. Kwon, K. Lee and J. S. Kim, *Adv. Funct. Mater.*, 2019, **29**, 1–9.
- 10 M. Zagórska, E. Taler, I. Kulszewicz-Bajer, A. Proń and J. Nizioł, *J. Appl. Polym. Sci.*, 1999, **73**, 1423–1426.
- 11 W. Yu, L. Zhou, S. Yu, P. Fu, X. Guo and C. Li, *Org. Electron.*, 2017, **42**, 387–392.
- 12 S. Che, R. Dao, W. Zhang, X. Lv, H. Li and C. Wang, *Chem. Commun.*, 2017, **53**, 3862–3865.
- 13 T. Welton, *Chem. Rev.*, 1999, **99**, 2071–2083.
- 14 M. Suh, J. Bailey, S. W. Kim, K. Kim, D. J. Yun, Y. Jung, I. Hamilton, N. Chander, X. Wang, D. D. C. Bradley, D. Y. Jeon and J. S. Kim, *ACS Appl. Mater. Interfaces*, 2015, **7**, 26566–26571.
- 15 N. Persson, M. McBride, M. Grover and E. Reichmanis, *Curr. Opin. Solid State Mater. Sci.*, 2016, **20**, 338–343.
- 16 M. Trznadel, A. Pron, M. Zagorska, R. Chrzaszcz and J. Pielichowski, *Macromolecules*, 1998, **31**, 5051–5058.
- 17 R. Mauer, M. Kastler and F. Laquai, *Adv. Funct. Mater.*, 2010, **20**, 2085–2092.
- 18 A. Zen, J. Pflaum, S. Hirschmann, W. Zhuang, F. Jaiser, U. Asawapirom, J. P. Rabe, U. Scherf and D. Neher, *Adv. Funct. Mater.*, 2004, **14**, 757–764.
- 19 R. J. Kline, M. D. McGehee, E. N. Kadnikova, J. Liu, J. M. J. Fréchet and M. F. Toney, *Macromolecules*, 2005, **38**, 3312–3319.
- 20 J. Clark, J. F. Chang, F. C. Spano, R. H. Friend and C. Silva, *Appl. Phys. Lett.*, 2009, **94**, 3–6.
- 21 F. C. Spano and C. Silva, *Annu. Rev. Phys. Chem.*, 2014, **65**, 477–500.
- 22 E. Tan, A. M. Pappa, C. Pitsalidis, J. Nightingale, S. Wood, F. A. Castro, R. M. Owens and J. S. Kim, *Biotechnol. Bioeng.*, 2020, **117**, 291–299.
- 23 J. Nightingale, J. Wade, D. Moia, J. Nelson and J. S. Kim, *J. Phys. Chem. C*, 2018, **122**, 29129–29140.
- 24 K. H. Yim, G. L. Whiting, C. E. Murphy, J. J. M. Halls, J. H. Burroughes, R. H. Friend and J. S. Kim, *Adv. Mater.*, 2008, **20**, 3319–3324.
- 25 W. C. Tsoi, D. T. James, J. S. J. S. Kim, P. G. Nicholson, C. E. Murphy, D. D. C. Bradley, J. Nelson and J. S. J. S. Kim, *J. Am. Chem. Soc.*, 2011, **133**, 9834–9843.
- 26 J. Razzell-Hollis, S. Limbu and J. S. Kim, *J. Phys. Chem. C*, 2016, **120**, 10806–10814.
- 27 A. N. Mallya, R. Kottokkaran and P. C. Ramamurthy, *Sens. Actuators, B*, 2014, **201**, 308–320.
- 28 A. Lv, Y. Pan and L. Chi, *Sensors*, 2017, **17**, 213.
- 29 D. T. Simon, E. O. Gabrielsson, K. Tybrandt and M. Berggren, *Chem. Rev.*, 2016, **116**, 13009–13041.
- 30 C. Bartic and G. Borghs, *Anal. Bioanal. Chem.*, 2006, **384**, 354–365.
- 31 F. P. V. Koch, J. Rivnay, S. Foster, C. Müller, J. M. Downing, E. Buchaca-Domingo, P. Westacott, L. Yu, M. Yuan, M. Baklar, Z. Fei, C. Luscombe, M. A. McLachlan, M. Heeney, G. Rumbles, C. Silva, A. Salleo, J. Nelson, P. Smith and N. Stingelin, *Prog. Polym. Sci.*, 2013, **38**, 1978–1989.
- 32 L. Pauling, A. B. Robinson, R. Teranishi and P. Cary, *Proc. Natl. Acad. Sci. U. S. A.*, 1971, **68**, 2374–2376.
- 33 M. Phillips, *Sci. Am.*, 1992, **267**, 74–79.
- 34 K. Staszek, A. Rydosz, E. Maciak, K. Wincza and S. Gruszczynski, *Sens. Actuators, B*, 2017, **245**, 882–894.
- 35 G. Peng, U. Tisch, O. Adams, M. Hakim, N. Shehada, Y. Y. Broza, S. Billan, R. Abdah-Bortnyak, A. Kuten and H. Haick, *Nat. Nanotechnol.*, 2009, **4**, 669–673.
- 36 J. Luke, E. M. Speller, A. Wadsworth, M. F. Wyatt, S. Dimitrov, H. K. H. Lee, Z. Li, W. C. Tsoi, I. McCulloch, D. Bagnis, J. R. Durrant and J. S. Kim, *Adv. Energy Mater.*, 2019, **9**, 1–14.
- 37 S. Limbu, S. Pont, A. B. Doust, S. Kwon, P. Fuller, E. Tan, J. R. Durrant and J. S. Kim, *Adv. Mater. Interfaces*, 2019, **6**, 1–10.
- 38 W. C. Tsoi, D. T. James, J. S. Kim, P. G. Nicholson, C. E. Murphy, D. D. C. Bradley, J. Nelson and J. S. Kim, *J. Am. Chem. Soc.*, 2011, **133**, 9834–9843.
- 39 S. Wood, J. R. Hollis and J. S. Kim, *J. Phys. D: Appl. Phys.*, 2017, **50**, 073001.
- 40 J. Yin, Z. Wang, D. Fazzi, Z. Shen and C. Soci, *J. Phys. Chem. C*, 2016, **120**, 1994–2001.
- 41 V. Hernandez, C. Castiglioni, M. Del Zoppo and G. Zerbi, *Phys. Rev. B: Condens. Matter Mater. Phys.*, 1994, **50**, 9815–9823.
- 42 C. Enengl, S. Enengl, S. Pluczyk, M. Havlicek, M. Lapkowski, H. Neugebauer and E. Ehrenfreund, *ChemPhysChem*, 2016, **17**, 3836–3844.
- 43 W. C. Tsoi, D. T. James, E. B. Domingo, J. S. Kim, M. Al-Hashimi, C. E. Murphy, N. Stingelin, M. Heeney and J. S. Kim, *ACS Nano*, 2012, **6**, 9646–9656.
- 44 G. S. Ryu, B. Nketia-Yawson, E. Y. Choi and Y. Y. Noh, *Org. Electron.*, 2017, **51**, 264–268.
- 45 R. Di Pietro and H. Sirringhaus, *Adv. Mater.*, 2012, 3367–3372.

